A TUNABLE MAST VIBRATION ABSORBER FOR VARIABLE RPM ROTORCRAFT

Luigi M. Bottasso, Luca Medici, Gian Vittorio Bernardi, Ermanno Fosco
Leonardo Helicopters
21017 Cascina Costa di Samarate (VA)
Italy

Abstract

We designed and tested the prototype of an adaptive Mast Vibration Absorber (MVA) which can be tuned at different frequencies, aimed at use on variable rpm rotorcraft. The proposed solution offers a monolithic design with virtually no moving parts. The resonance frequency is tuned by controlling the compressive load in the MVA support beam; compression tends to destabilize a beam and thus reduces its natural frequency. With no need for reconfiguration mechanisms involving mass displacement, the proposed approach preserves the typical rugged design and very low damping characteristics of standard fixed-frequency MVAs. We designed, built and tested a laboratory demonstrator broadly representative of a real application in terms of dynamical properties and geometrical constraints, aimed at verifying the concept and evaluating practical implementation issues such as system efficiency, size and actuation requirements.

1 INTRODUCTION

A mast vibration absorber (MVA) is a mass damper mounted on the N-bladed main rotor of a helicopter, and rotating with it, aimed at reducing the in-plane components of the vibratory loads before they are transmitted through the hub to the helicopter cabin.

The main function of the MVA is to create an antiresonance in correspondence of its natural frequency, which is tuned to the same N/rev frequency of the disturbance that needs to be attenuated in the fixed frame. Figure 1 shows the MVA installation on the main rotor of the AW139 helicopter.
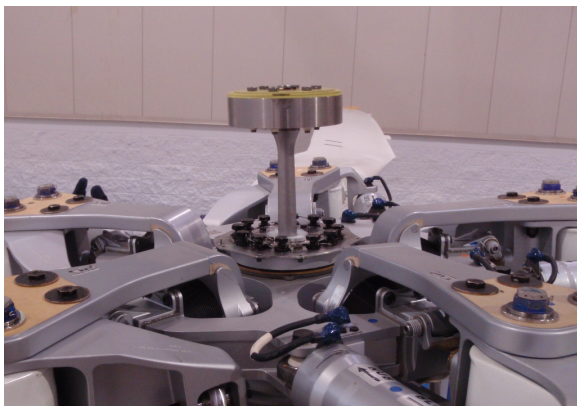
Figure 1: AW139 MVA assembly

It shall be remarked that the anti-resonance tuning above described is strictly optimal only for a one degree of freedom system excited by a single loading component, which is not what happens on a helicopter rotor. In-fact the rotor generates three force components and three moment components on the hub, each with different phases and amplitudes. Under these circumstances, the MVA tuning at the N/rev might not be necessarily the best choice, but simply a trade-off between simplicity and performance.

Considering the in-plane components of the vibratory loads generated by an N-bladed rotor spinning at 1/rev, we find that the harmonics which excite the MVA in the rotating frame are those at (N-1)/rev and (N+1)/rev (and multiples). However, moving the perspective to the fixed frame, we observe a frequency shift so that the excitation is transmitted to the helicopter at N/rev (and multiples).

This fact can be better visualized if we consider the following equivalent model of the MVA. Let's assume the stationary rotor case; the inertial force generated by the MVA mass oscillating at N/rev in the xy rotor plane is equivalent to the combined effect of two eccentric masses spinning around the rotor mast in opposite directions at +N/rev and -N/rev respectively.

Under these circumstances, the force vector describes an elliptic path on the xy plane, degenerating to a straight line if the masses and their eccentricities are equal. Introducing the rotor rotation at 1/rev, one mass is spinning in the same direction as the rotor, while the other in the opposite direction, thus one at (N+1)/rev, the other at (N-1)/rev.

Plotting the path of the resultant force vector we observe a figure with N lobes which graphically shows the N/rev excitation exerted by the two-mass system, and thus by the MVA, on the fixed frame. Figure 2 illustrates the MVA path evolution during one rotation of the rotor.

Like all tuned mass dampers, MVAs are highly effective only at the tuning frequency, while their effect becomes poor or negligible outside a very narrow band. An MVA is pro-

vided with as little damping as possible in order to maximize its efficiency at the tuning frequency of interest, effectively operating as a notch filter.
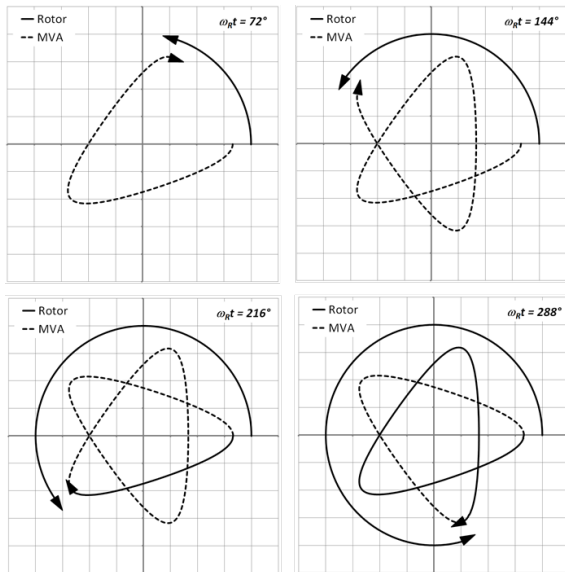
Figure 2: MVA oscillation path after $1/5^{th}$, $2/5^{th}$, $3/5^{th}$ and $4/5^{th}$ of a full rotation of the rotor spinning at ω_R

As a simple illustrative example, Figure 3 shows the response of a single degree of freedom tuned mass damper which is interpreted here as a schematic model of a notional helicopter rotor head and associated MVA. The key parameters are:

m = 400 kg: mass of rotor + hub + mast
m_d = 20 kg: mass of damper
ξ = 0.015: rotor structure damping ratio
ξ_d = 0.001: MVA damping ratio
f = 15 Hz: structure frequency (e.g. 1st mast harmonic)
f_d = 24.9 Hz: damper tuning frequency
p = 6 kN: amplitude of rotor forcing load
$1/rev$ = 4.98 Hz (298.8 rpm)
N = 5 blades

Under the above circumstances, a perfectly tuned MVA is able to cancel the rotor vibration with an oscillation amplitude of about $\pm$ 12 mm. However, with a de-tuning of even a fraction of Hz the benefits vanish; the MVA can actually amplify vibration if its displacement amplitude is not restrained through an endstop.

Current MVA devices are designed as simple cantilever beam systems with an end fixed at the rotor hub and the oscillating mass on the opposite end.
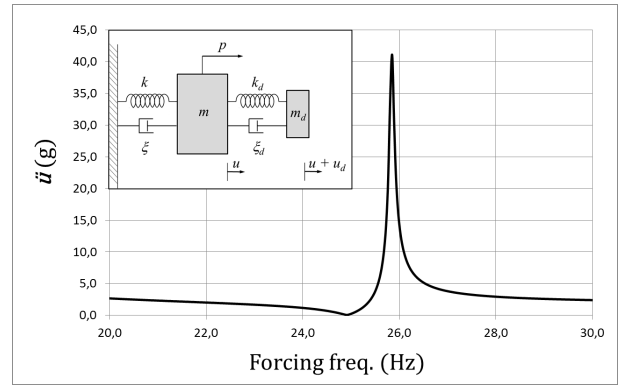
Figure 3: Damped response of a schematic rotor-head

The system is very simple and effective, however its major limitation consists in its inability to adjust to a changing forcing frequency, a need which naturally arises in a variable-rpm helicopter. Various active vibration reduction solutions have been explored to overcome this limitation (an overview is contained in[1]).

A device which effectively represents an active analogue of a tuned damper is based on counter-rotating masses, essentially centrifugal force generators which can produce force vectors in the rotor plane. However, the higher complexity, cost and maintenance requirements of these systems represent possible areas of concern.

The hub of a helicopter constitutes a very harsh environment for any vibration suppression device. This is primarily a consequence of the high vibration amplitudes necessary for an effective vibration damping function, which can quickly lead to unacceptably high levels of fatigue damage.

An almost intuitive way to design a tunable device would consist in providing some form of variable geometry features, e.g. through moving masses and associated sliding contact surfaces, guides or hinges. However, in general these mechanisms would lead to fretting, backlash and thus fatigue in a high-g vibratory environment, with an associated increase in damping and reduced effectiveness.

A monolithic construction with no moving parts is therefore a desirable feature for any hub-mounted vibration suppression system.

2 PROPOSED SOLUTION

A possible alternative approach being proposed here consists in a tunable adaptive MVA system, which combines a relatively simple monolithic design, lack of rotating inertial masses and an intrinsic ability to cope with variable rpm.

The goal is achieved through a design whereby the MVA support beam can be subjected to compression / tension, thus altering its fundamental frequency and effectively allowing the tuning of the beam. Compressive loads have a destabilizing effect and thus reduce the resonance frequency while tension has a stabilizing effect and increases the frequency (as is well known in the field of string musical instruments).

The above task is somehow simplified in the context of the helicopter MVA application because the tuning range required to cope with variable rpm is not very large. As an example, the variable-rpm helicopter AW169 operates within a 7% rpm range, from 96% to 103% of nominal rpm.

Figure 4 shows a schematic cantilever beam system with tip mass under compressive load.
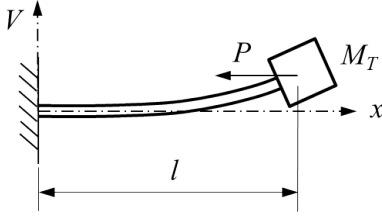
Figure 4: Cantilever beam with tip mass under constant axial load

With reference to Figure 4 and ignoring the axial load P, the frequency of the beam's 1st bending mode is given by

$$\omega = \sqrt{\frac{3EJ}{M_T l^3}}$$

Where EJ is the beam's bending stiffness

Accounting for the distributed mass of the beam, assuming a linear mass density ρ, the expression is modified as [2]

$$\omega = \sqrt{\frac{3EJ}{(0.2235\rho l + M_T)l^3}}$$

A change of ω can be achieved through the application of a preload on the beam; with compression the frequency decreases while if tension is applied the frequency increases. The intuitive explanation is that a compressive load tends to oppose the elastic restoring moment. At the limit, the frequency tends to zero when the compressive load P reaches the critical (Euler) buckling load which destabilizes the cantilever beam

$$P_{cr} = \frac{\pi^2 EJ}{4l^2}$$

2.1 Remarks on Alternative Solutions

Looking at alternative tuning solutions able to preserve the monolithic requirement, one could in principle consider some form of variable stiffness, for example using magnetorheological (MR) fluids or piezo-patches embedded in the MVA support beam. MR fluid-filled tunable beams have been demonstrated [3] [4], furthermore MR fluid dampers are being designed for civil applications [5]. However this approach would not be suitable for the MVA case where we need a combination of high stiffness in a thin element. MR fluids properties [6] [7] in terms of Young's modulus ($\sim$10 MPa) and yield stress (50-100 kPa) are much too low to have a noticeable effect on the support beam made of high-strength steel (200 GPa Young's modulus, >1000 MPa yield

stress). Filling the MVA support tube with MR fluid would alter its bending stiffness by a negligible amount.

On the other hand, piezo patches embedded in the support beam material could conceivably generate a pre-stress state and thus somehow alter the dynamic properties of the element; however piezo-ceramic materials are notoriously brittle and would represent a weak area under repeated vibrations.

In light of the above observations and considering the specific application at hand, our conclusion is that the only practical way to obtain a useful frequency variation in a monolithic, highly stiff MVA device is through a "brute force" approach, i.e. applying rather large axial loads, as will be described in the paper.

2.2 End Mass Effects

The scheme presented above is strictly valid in the case of a point mass attached to the free end of the cantilever beam. The reality of a typical Mast Vibration Absorber deviates from this idealized situation due to the relatively large mass and the associated rotational inertia which cannot be completely neglected, despite the use of high density materials such as tungsten having ρ = 19250 kg/m^3, almost 2.5 times higher than steel.
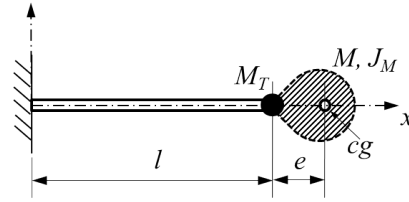
Figure 5: Replacement of end mass and inertia with effective concentrated mass at beam tip

Assuming the scheme of Figure 5, an effective lumped mass which preserves the frequency response characteristics of the system is computed as presented in [8]

$$(1) \qquad M_T = M\left[(1+3\bar{e}) + \frac{9}{4}(\bar{e}^2 + \bar{J}_M)\right]$$

where M is the mass at the free end of the cantilever, with eccentricity e and inertia J_M, and defining the associated non-dimensional parameters $\bar{e} = e/l$, $\bar{J}_M = J_M/Ml^2$.

3 THEORETICAL JUSTIFICATION

3.1 Free Vibration in the Euler-Bernoulli Beam

Looking at the analytical model of the cantilever beam with tip mass and compressive load [9] [10] [11] illustrated in Figure 4, we define the following variables:

EJ: beam bending stiffness

ρ: linear density of the beam (mass per unit length)

l: beam length

P: axial load

k: axial load parameter, $\sqrt{P/EJ}$

$\bar{k}$: nondimensional axial load parameter, $\sqrt{Pl^2/EJ}$

β: frequency parameter, $\sqrt[4]{\rho\omega^2/EJ}$

$\bar{\beta}$: nondimensional frequency parameter, βl

M_T: tip effective mass, inclusive of inertia effect

M_B: total mass of the beam, ρl

η_T: ratio of tip mass to total beam mass, M_T/M_B

$v(x)$: beam displacement

$\bar{v}(x)$: nondimensional beam displacement, v/l

x: lengthwise coordinate

$\bar{x}$: nondimensional lengthwise coordinate, x/l

ω: circular frequency of vibration

Let's assume a uniform beam of linear density ρ in free vibration and under the axial load P as illustrated in Figure 6
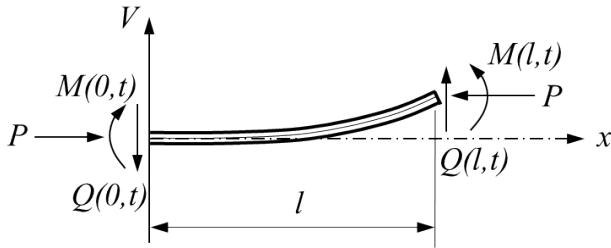
Figure 6: Coordinate system
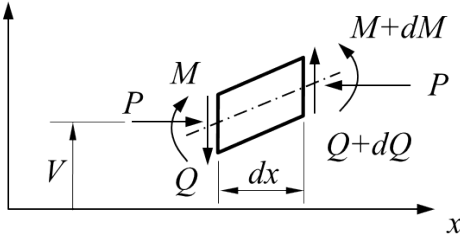
Figure 7: Cantilever beam with tip mass under constant axial load

Let $V(x,t)$ be the displacement of a point at coordinate x along the beam neutral axis. Considering the beam element illustrated in Figure 7 and the equilibrium of forces and moments, two equations can be written

$$(2) \qquad \frac{\partial Q(x,t)}{\partial x} - \rho \frac{\partial^2 V(x,t)}{\partial t^2} = 0$$

$$(3) \qquad \frac{\partial M(x,t)}{\partial x} + P\frac{\partial V(x,t)}{\partial x} + Q(x,t) = 0$$

The bending moment as a function of curvature can be expressed as

$$(4) \qquad M(x,t) = EJ\frac{\partial^2 V(x,t)}{\partial x^2}$$

By combining equations 3 and 4 it is possible to write an expression for shear

$$(5) \qquad Q(x,t) = -\left[EJ\frac{\partial^3 V(x,t)}{\partial x^3} + P\frac{\partial V(x,t)}{\partial x}\right]$$

Substituting 5 in 2, the resulting equation of motion of the beam in terms of the displacement $V(x,t)$ is obtained

$$(6) \qquad \frac{\partial^4 V(x,t)}{\partial x^4} + \frac{P}{EJ}\frac{\partial^2 V(x,t)}{\partial x^2} + \frac{\rho}{EJ}\frac{\partial^2 V(x,t)}{\partial t^2} = 0$$

We assume a harmonic solution for the displacement, shear and moment, thus having the form:

$$(7) \qquad V(x,t) = v(x)e^{i\omega t}$$

$$(8) \qquad Q(x,t) = q(x)e^{i\omega t}$$

$$(9) \qquad M(x,t) = m(x)e^{i\omega t}$$

After substitution of 7 in 6, then dividing by $e^{i\omega t}$ and defining

$$k^2 = \frac{P}{EJ} \qquad \beta^4 = \frac{\rho\omega^2}{EJ}$$

The equation of motion 6 becomes

$$(10) \qquad \frac{d^4v(x)}{dx^4} + k^2\frac{d^2v(x)}{dx^2} - \beta^4 v(x) = 0$$

And the time-independent expressions for shear and moment are

$$(11) \qquad m(x) = EJ\frac{d^2v(x)}{dx^2}$$

$$(12) \qquad q(x) = -EJ\left[\frac{d^3v(x)}{dx^3} + k^2\frac{dv(x)}{dx}\right]$$

Furthermore, by defining

$$\bar{x} = \frac{x}{l} \qquad \bar{v} = \frac{v}{l} \qquad \bar{k} = kl \qquad \bar{\beta} = \beta l$$

equations 10 11 12 can be transformed into a nondimensional form

$$(13) \qquad \frac{d^4\bar{v}(\bar{x})}{d\bar{x}^4} + \bar{k}^2\frac{d^2\bar{v}(\bar{x})}{d\bar{x}^2} - \bar{\beta}^4 \bar{v}(\bar{x}) = 0$$

$$m(\bar{x}) = \frac{EJ}{l}\frac{d^2\bar{v}(\bar{x})}{d\bar{x}^2}$$

(15) $$q(\bar{x}) = -\frac{EJ}{l^2}\left[\frac{d^3\bar{v}(\bar{x})}{d\bar{x}^3} + \bar{k}^2\frac{d\bar{v}(\bar{x})}{d\bar{x}}\right]$$

The differential equation 13 admits the following general solution containing four constants A, B, C and D,

(16) $$\bar{v}(\bar{x}) = A\cosh(\alpha_1\bar{x}) + B\sinh(\alpha_1\bar{x})$$
$$+ C\cos(\alpha_2\bar{x}) + D\sin(\alpha_2\bar{x})$$

Where

$$\alpha_1 = \sqrt{-\frac{\bar{k}^2}{2} + \sqrt{\frac{\bar{k}^4}{4} + \bar{\beta}^4}}$$

$$\alpha_2 = \sqrt{\frac{\bar{k}^2}{2} + \sqrt{\frac{\bar{k}^4}{4} + \bar{\beta}^4}}$$

The boundary conditions for the beam clamped at one end are

$$\begin{cases} \bar{v}(\bar{x}) = 0 & \text{for } \bar{x} = 0 \\ \frac{d\bar{v}(\bar{x})}{d\bar{x}} = 0 & \text{for } \bar{x} = 0 \end{cases}$$

Applying the clamped end boundary conditions to equation 16 and knowing that

(17) $$\frac{d\bar{v}(\bar{x})}{d\bar{x}} = A\alpha_1\sinh(\alpha_1\bar{x}) + B\alpha_1\cosh(\alpha_1\bar{x})$$
$$- C\alpha_2\sin(\alpha_2\bar{x}) + D\alpha_2\cos(\alpha_2\bar{x})$$

We obtain the following relations which allow evaluation of two of the four constants

$$\begin{cases} A + C = 0 \\ \alpha_1 B + \alpha_2 D = 0 \end{cases}$$

Thus

$$\begin{cases} C = -A \\ D = -\frac{\alpha_1}{\alpha_2}B \end{cases}$$

The resulting solution for the beam clamped at $\bar{x} = 0$ is

(18) $$\bar{v}(\bar{x}) = A[\cosh(\alpha_1\bar{x}) - \cos(\alpha_2\bar{x})]$$
$$+ B\left[\sinh(\alpha_1\bar{x}) - \frac{\alpha_1}{\alpha_2}\sin(\alpha_2\bar{x})\right]$$
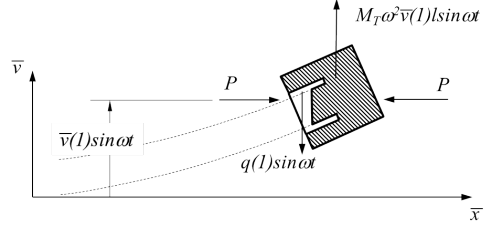
Figure 8: Equilibrium of forces at beam tip

The free end boundary condition at the beam tip ($\bar{x} = 1$) requires that both the bending moment and the shear force vanish; looking at Figure 8 and accounting for the concentrated mass M_T at the tip this implies

$$q(1) - M_T\omega^2\bar{v}(1)l = 0$$

Since $M_T = \eta_T M_B$ and $M_B = \rho l$ we obtain

$$q(1) - \eta_T\rho l^2\omega^2\bar{v}(1) = 0$$

By using equation 15

$$-\frac{EJ}{l^2}\left[\frac{d^3\bar{v}(1)}{d\bar{x}^3} + \bar{k}^2\frac{d\bar{v}(1)}{d\bar{x}}\right] - \eta_T\rho l^2\omega^2\bar{v}(1) = 0$$

and observing that $\rho l^2\omega^2 = \bar{\beta}^4 EJ/l^2$ we obtain

$$\frac{EJ}{l^2}\left[\frac{d^3\bar{v}(1)}{d\bar{x}^3} + \bar{k}^2\frac{d\bar{v}(1)}{d\bar{x}}\right] + \frac{\eta_T\bar{\beta}^4 EJ}{l^2}\bar{v}(1) = 0$$

simplifying

$$\frac{d^3\bar{v}(1)}{d\bar{x}^3} + \bar{k}^2\frac{d\bar{v}(1)}{d\bar{x}} + \eta_T\bar{\beta}^4\bar{v}(1) = 0$$

we can thus summarize the two boundary conditions at the free end

$$\begin{cases} \frac{d^2\bar{v}(\bar{x})}{d\bar{x}^2} = 0 & \text{for } \bar{x} = 1 \\ \frac{d^3\bar{v}(\bar{x})}{d\bar{x}^3} + \bar{k}^2\frac{d\bar{v}(\bar{x})}{d\bar{x}} + \eta_T\bar{\beta}^4\bar{v}(\bar{x}) = 0 & \text{for } \bar{x} = 1 \end{cases}$$

Applying the boundary conditions to equation 18 we obtain two homogeneous equations in A and B

$$\begin{cases} A(\alpha_1^2\cosh\alpha_1 + \alpha_2^2\cos\alpha_2) \\ + B(\alpha_1^2\sinh\alpha_1 + \bar{\beta}^2\sin\alpha_2) = 0 \\ \\ A[\alpha_2^2\sinh\alpha_1 - \bar{\beta}^2\sin\alpha_2 + \alpha_2\eta_T\bar{\beta}^2(\cosh\alpha_1 - \cos\alpha_2)] \\ + B[\alpha_2^2\cosh\alpha_1 + \alpha_1^2\cos\alpha_2 \\ + \eta_T\bar{\beta}^2(\alpha_2\sinh\alpha_1 - \alpha_1\sin\alpha_2)] = 0 \end{cases}$$

This is a homogeneous system of two algebraic equations in A and B; in order for the system to have non-zero solutions its determinant shall be zero, which leads to the associated characteristic equation expressing the linkage between the axial load (captured by $\bar{k}$) and the frequency of vibration (captured by $\bar{\beta}$):

$$-2\overline{\beta}^4 + \overline{\beta}^2\overline{k}^2 \sinh\alpha_1 \sin\alpha_2 - (2\overline{\beta}^4 + \overline{k}^4)\cosh\alpha_1 \cos\alpha_2$$
$$+ \eta_T\overline{\beta}^2(\alpha_1^2 + \alpha_2^2)(\alpha_1 \cosh\alpha_1 \sin\alpha_2$$
$$-\alpha_2 \sinh\alpha_1 \cos\alpha_2) = 0$$

(19)

Equation 19 is plotted in Figure 9 for different values of the parameter η_T [9], with positive P denoting compression
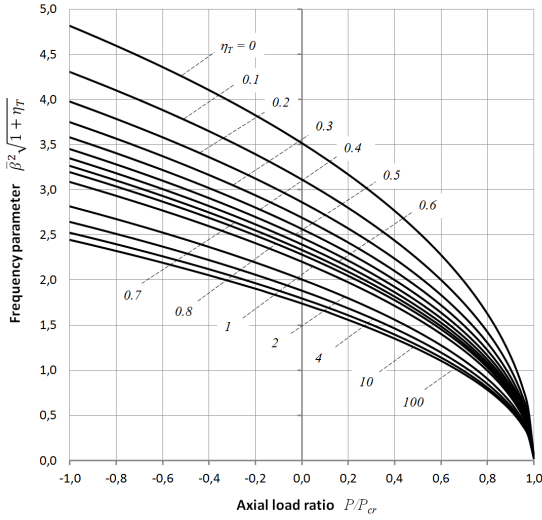
Figure 9: Frequency dependence on axial load for cantilever beam with tip mass

3.2 The Effect of Oblique Axial Load

Let's now consider the case when the axial load is not parallel to the undeformed beam axis [9] but oscillates with the beam, always directed towards a point along the beam axis. Under these assumptions the loading condition at the tip end is represented by Figure 10.
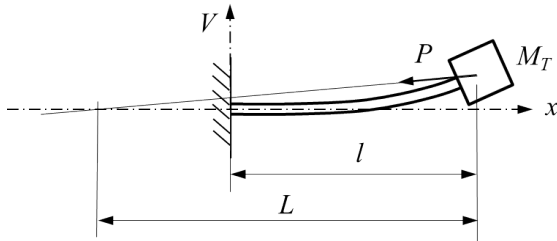
Figure 10: Cantilever beam with tip mass under oblique axial load
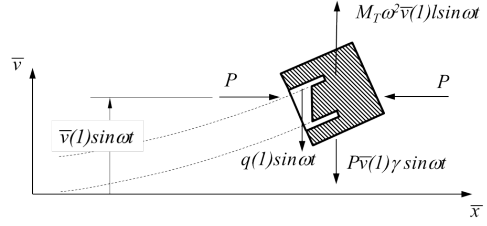
Figure 11: Equilibrium of forces at beam tip under oblique axial load

From Figures 10 and 11, the resulting boundary condition at the free end becomes

$$q(1) - M_T\omega^2\overline{v}(1)l + P\overline{v}(1)\gamma = 0$$

where $\gamma = l/L$ and L is the distance from the tip to the vertex of the oblique load, which is the point where its direction crosses the beam axis.

Knowing that

$$P = \frac{\overline{k}^2 EJ}{l^2}$$

We observe that the effect of the oblique load is to modify the second boundary condition at the free end through the factor $k^2\gamma$

$$\begin{cases} \dfrac{d^2\overline{v}(\overline{x})}{d\overline{x}^2} = 0 & \text{for } \overline{x} = 1 \\ \dfrac{d^3\overline{v}(\overline{x})}{d\overline{x}^3} + \overline{k}^2\dfrac{d\overline{v}(\overline{x})}{d\overline{x}} + (\eta_T\overline{\beta}^4 - \overline{k}^2\gamma)\overline{v}(\overline{x}) = 0 & \text{for } \overline{x} = 1 \end{cases}$$

Leading to the reformulation of the characteristic equation

$$-2\overline{\beta}^6 + \overline{\beta}^4\overline{k}^2 \sinh\alpha_1 \sin\alpha_2 - \overline{\beta}^2(2\overline{\beta}^4 + \overline{k}^4)\cosh\alpha_1 \cos\alpha_2$$
$$+ (\eta_T\overline{\beta}^4 - \overline{k}^2\gamma)(\alpha_1^2 + \alpha_2^2)(\alpha_1 \cosh\alpha_1 \sin\alpha_2$$
$$-\alpha_2 \sinh\alpha_1 \cos\alpha_2) = 0$$

(20)

Equation 20 is plotted in Figure 12 for different values of the parameter η_T [9], assuming the condition where the load P is directed towards the beam's fixed end, thus with $\gamma = 1$.
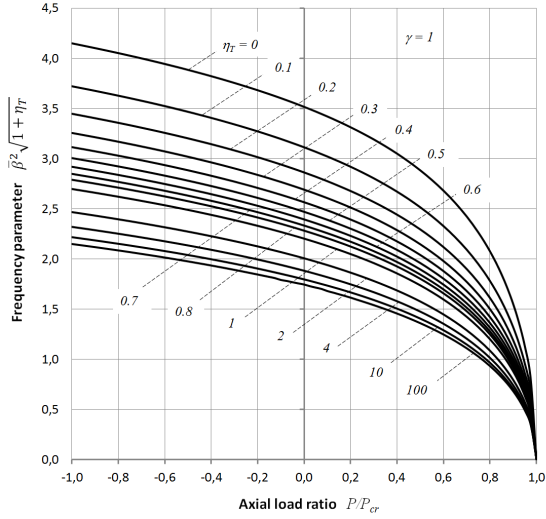
Figure 12: Frequency dependence on oblique axial load for cantilever beam with tip mass ($\gamma = 1$)

The oblique compressive load case is less efficient than the parallel load case in terms of its frequency reduction capability. This is because the oblique force has a component which tends to re-stabilize the beam, thus altering the boundary condition at the free end. The new boundary condition reduces the beam's effective length factor thus increasing its critical load, resulting in reduced tuning effectiveness.

This fact is illustrated in Figure 13 where we plot the frequency variation as a function of the load for different values of γ but this time normalizing the load to the critical load P_{cr}^0 of the case $\gamma = 0$, i.e. with vertical load.
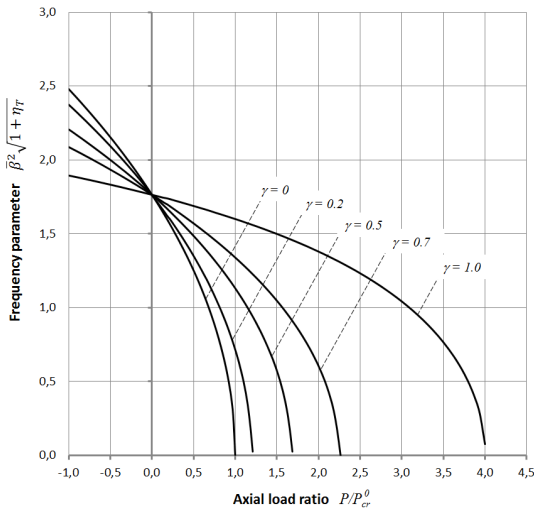
Figure 13: Loss of effectiveness of axial load frequency tuning with increasing values of γ; here we plot on the x-axis the ratio of the axial load to the critical load associated with the vertical load case with $\gamma = 0$ (all cases plotted have $\eta_T = 20$)

Clearly, when $\gamma \to 0$ the loading condition converges on

the parallel load case and equation 20 becomes 19.

The oblique axial load case of Figure 10 is of practical interest because it can be more easily implemented in a real device, e.g. as illustrated in Figure 14 where a tubular element contains a string-like tension link oscillating within the tube without contact.

This concept can work under the assumption of small vibration amplitude, which is consistent with an MVA case.
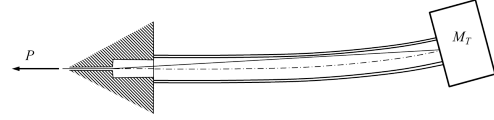
Figure 14: Practical implementation of the oblique loading scheme

3.3 The Effect of Centrifugal Acceleration

Let's assume the beam is rotating around its neutral axis with circular frequency ω_r; we neglect the centrifugal effect on the distributed mass of the beam because in the case under study the tip mass is at least an order of magnitude larger. Thus the tip mass is subject to the centrifugal force

$$F = M_T \omega_r^2 V(l,t) = M_T \omega_r^2 v(l) e^{i\omega t}$$

The scheme is illustrated in Figure 15
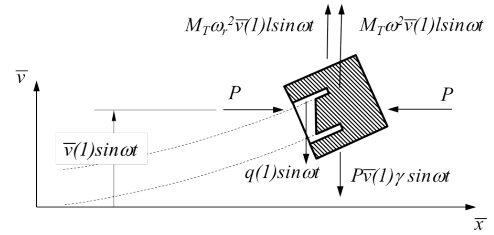
Figure 15: Equilibrium of forces at beam tip under oblique axial load and centrifugal effect

We define the non-dimensional parameter

$$\beta_r^4 = \frac{\rho \omega_r^2}{EJ} \qquad with \quad \overline{\beta}_r = \beta_r l$$

We thus obtain a new tip load component similar in form to the inertial component considered previously. The modified tip loading conditions lead to a modified characteristic equation accounting both for the oblique axial load and for the centrifugal acceleration at the tip mass due to the beam's rotation around its axis

$$-2\overline{\beta}^6 + \overline{\beta}^4 \overline{k}^2 \sinh\alpha_1 \sin\alpha_2 - \overline{\beta}^2 (2\overline{\beta}^4 + \overline{k}^4) \cosh\alpha_1 \cos\alpha_2$$
$$+ (\eta_T(\overline{\beta}^4 + \overline{\beta}_r^4) - \overline{k}^2 \gamma)(\alpha_1^2 + \alpha_2^2)(\alpha_1 \cosh\alpha_1 \sin\alpha_2$$
$$- \alpha_2 \sinh\alpha_1 \cos\alpha_2) = 0$$

(21)

4 EXPERIMENTAL VERIFICATION

An experimental device was designed and built, to be used as a laboratory demonstrator of a helicopter TMVA. A section view of the device's layout is illustrated in Figure 16, while Figures 17, 18 illustrate the TMVA demonstrator disassembled and assembled. The as-built device characteristics were:

Support beam: steel tube $\emptyset_{ext}$ = 28.7 mm, thk = 4.85 mm
ρ = 2.83 kg/m
l = 321 mm
M_B = 0.91 kg
M_T = 15.9 kg (effective mass incl. inertia effect)
η_T = 17.48

which lead to the expected free vibration frequency ω = 173.15 rad/s = 27.56 Hz.

A certain discrepancy between predicted and measured frequencies can be explained both by uncertainties in the material Young's modulus and by the (small) elasticity of the test rig. Specifically, the latter was slightly different for horizontal and vertical vibrations, due to the particular geometry of the installation.

Tension was provided through a high-strength steel cable of the type used for lifting equipment ($\emptyset$ = 8 mm) with threaded (M12) terminals, as illustrated in Figures 18 and 19.

In order to reduce the angular oscillation of the cable, and thus approach the ideal case where the compressive force is parallel to the undeformed beam axis, the cable length was set as twice that of the cantilever beam, leading to a nominal γ = 0.5. Figure 20 shows the device on its test rig, complete with a 3-axis accelerometer on the tip mass.

For simplicity, tension was applied by manually tightening a nut on the threaded cable terminal with a torque-wrench, and a load cell was used to measure the applied load.

To prevent uncontrolled vibration of the cable inside the TMVA support tube, it is necessary to avoid resonance between the cable 1st harmonic and the oscillatory motion of the TMVA. The cable characteristics are reported below:

L = 0.64 m
$\emptyset$ = 8 mm
ρ_c = 0.32 kg/m (linear density)

The frequency of the 1st harmonic can be obtained by Mersenne's law for a stretched string (used for the tuning of musical instruments):

$$(22) \qquad f = \frac{1}{2L}\sqrt{\frac{F}{\rho_c}}$$

where F is the tension in the string.

Applying 22 to our cable geometry leads to the need for $F \geq 500$ N to avoid having f too close to the 27.56 Hz frequency of the forcing oscillation. At the opposite extreme, a value of F = 35 kN leads to f = 258 Hz.

Figure 16: Scheme of a tunable MVA for ground test concept demonstration

Figure 17: The disassembled TMVA demonstrator

Figure 18: The assembled TMVA demonstrator and the tension cable with terminals

Figure 19: Close up of a threaded terminal

Figure 22: View of the piezoelectric load cell and the torque nut on the cable terminal

Figure 20: The TMVA on the test rig

Figure 21 illustrates the accelerometer installed on the tip mass, with indicated the vertical and horizontal acceleration components (these would represent the in-plane vibration directions in a helicopter rotor application). Figure 22 illustrates the opposite end of the TMVA, with the nut used for torque application and the piezoelectric load cell between washers.
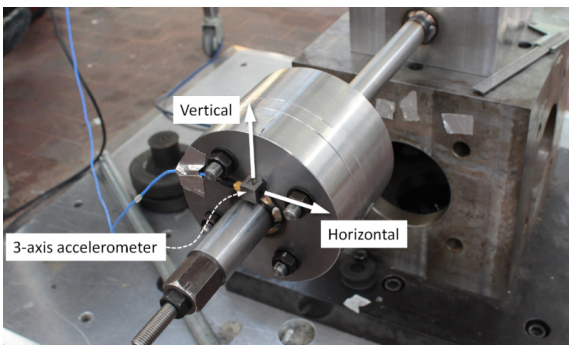
Figure 21: 3-axis accelerometer on tip mass
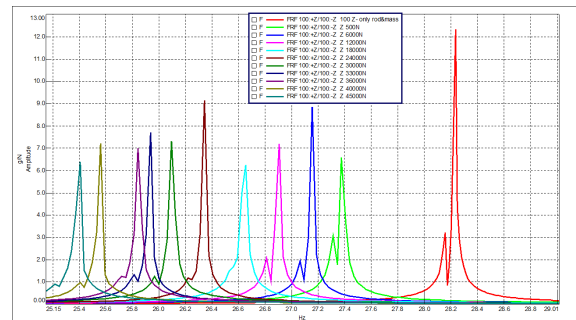
Figure 23: FRF plots for the various load cases analyzed

A rap-test was conducted with the use of an instrumented hammer. The direction of impact was not precisely controlled, resulting in the tip mass response having both a vertical and a horizontal component. The slight difference in stiffness of the test rig in the two directions led to resulting small differences (0.07 - 0.10 Hz) in the associated characteristic frequencies. This was evident in the frequency response function (FRF) plots where two closely spaced peaks are clearly visible for each value of tension load, see diagrams in Figure 23.

Recall that FRF is defined as the ratio of the complex spectrum of the response to the complex spectrum of the excitation

$$(23) \qquad FRF = H(f) = \frac{X(f)}{F(f)}$$

Table 1 shows the data points from the TMVA tests. The data confirm that the relation between the applied torque T, and the axial load P follows the typical formula used for bolts:

$$T = k_f PD$$

Where D is the bolt thread diameter and k_f is a factor dependent on friction. In our case we observed k_f = 0.16, a value typical of lubricated contact.

More importantly, the data show that a 2 Hz frequency variation was achieved at a compression load of 45 kN, with virtually no impact on the system's damping ratio ξ, which

remained very low throughout the test and unaffected by the tuning mechanism.

Figure 24 overlays the results of the experimental test with the theoretical predictions for γ = 0.5 and for γ = 0.7. Figure 25 shows a close-up of the previous plot in the load range explored, which is approximately linear.

Table 1: Experimental results

Torque	Load	Elong.	Freq.	Damping
Nm	N	mm	Hz	%
1.0	500	0.0	27.38	0.06
11.5	6000	1.1	27.16	0.05
23.0	12000	2.0	26.91	0.06
34.6	18000	2.8	26.66	0.08
46.1	24000	3.2	26.34	0.05
57.6	30000	3.9	26.09	0.07
63.4	33000	4.2	25.94	0.05
69.1	36000	4.9	25.84	0.07
76.8	40000	5.1	25.56	0.05
86.4	45000	5.5	25.41	0.07

The plot shows that the experimental data are in agreement with the curve γ = 0.7. This can be explained considering that the steel cable, despite its flexibility, cannot behave as an ideal string-like element. The curvature radius of the cable at the crimped terminals reduces its effective length and thus increases the value of γ, resulting in a reduction of the frequency-tuning capability. The effect is depicted in figure 26 for clarification. A better implementation would require switching from a conventional steel cable to a carbon fiber cable of the type used for special lifting applications.
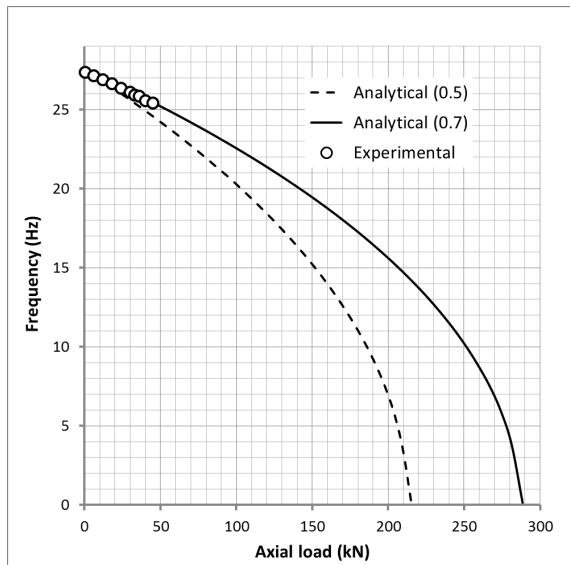
Figure 24: Frequency shift as a function of axial load: comparison of experimental data with two analytical cases (γ = 0.5 and γ = 0.7)

This new tension element would combine higher strength, reduced thickness and increased bending flexibility, making it much more similar to the ideal string of the

analytical solution. We expect that, with these improvements, the frequency vs load plot would approach much more closely the curve for γ = 0.5, thus allowing the same 2-Hz tuning range with a tension load of 35 kN rather than 45 kN as was the case of our experiment.
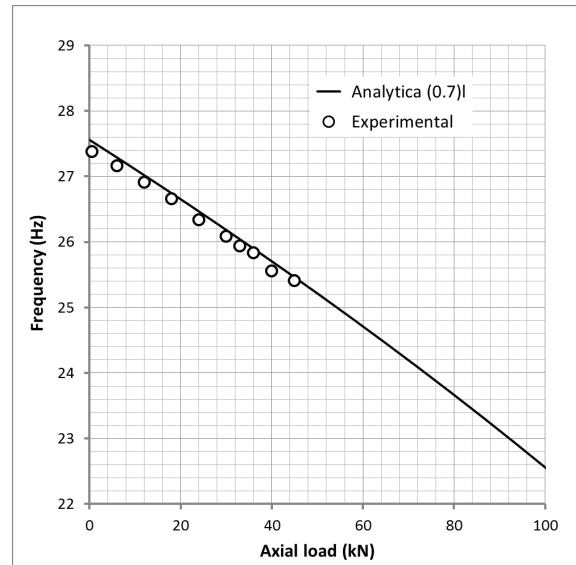
Figure 25: Frequency shift as a function of axial load: experimental data match the analytical case for γ = 0.7
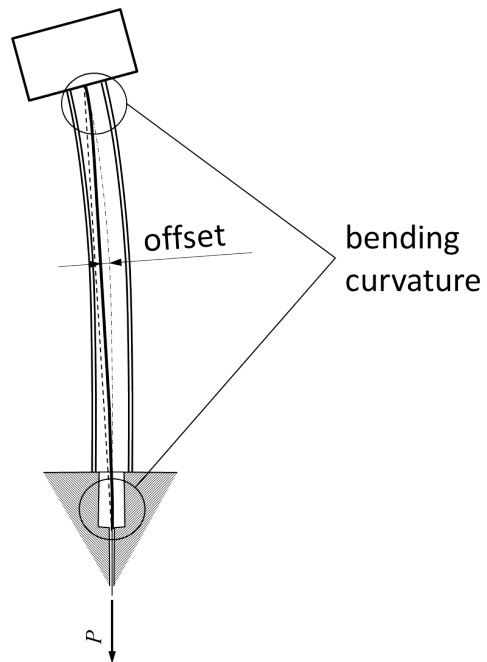
Figure 26: Bending curvature at the tension link terminals reduces the offset and thus the destabilizing bending moment of the axial load P (the dotted line is the ideal case for a string-like element having only tensile axial stiffness)

The above geometry and dynamical properties were designed to provide useful vibration amplitude at the tip, this

feature being directly linked to the force generation capability of the vibration absorber. The 5.5 mm gap between the Ø 8 mm cable and the $Ø_{int}$ 19 mm tube is sufficient to accommodate a tip vibration amplitude of over ±9 mm without contact, as illustrated in Figure 27. Under these conditions the cable oscillates by a mere ±0.8 deg.
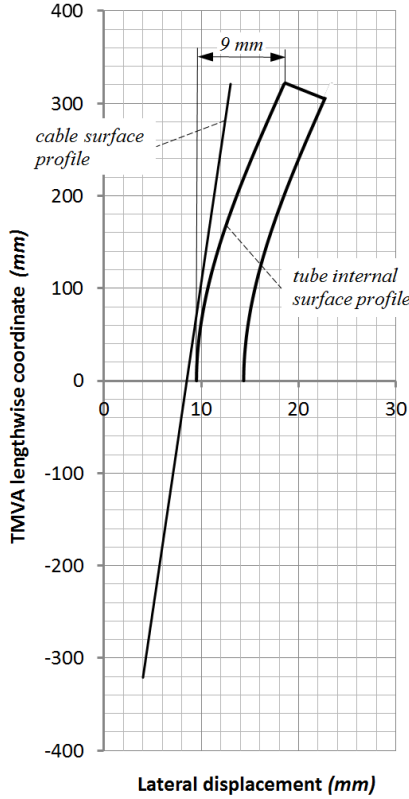
Figure 27: Profile of the deflected TMVA tube and inner cable under a 9 mm tip displacement (horizontal coordinate is amplified 10X for clarity)

The resulting inertial force amplitude is computed as

$d = ±9$ mm (tip vibration amplitude)
$a = \omega^2 d = ±27.5$ g (tip acceleration at 27.56 Hz)
$F = M_T a = ±4290$ N (inertial force)

5 CONCLUSIONS AND NEXT STEPS

The experimental setup described in this paper is broadly representative of a rotorcraft application in terms of dynamic characteristics, tuning range, overall geometry, size and mass. However, a real installation would require substantial improvements in several areas.

First of all the MVA support beam cannot be a constant cross section tube but shall be tapered for stress optimization. In the experiment described it was natural to adopt this simplification because it is the only configuration for which a rigorous analytical solution of the characteristic equation can be obtained with reasonable simplicity. Just by adding a linearly tapered section the mathematical complexity increases sharply, with no real benefit in terms of proving the principle.

Assuming an operational tip load F = 4290 N (corresponding to a peak acceleration of 27.5 g for the 15.9 kg mass), our MVA demonstrator design would lead to a nominal bending stress (i.e. without considering stress concentration factors) of ±734 MPa at the beam root, well above the fatigue limit of the typical materials used for this application (∼500 MPa for stainless steel 17-4 PH). While this was acceptable for test purposes, obviously the detailed design will require finite element modelling in order to converge on a balanced configuration ensuring optimized stress distribution and at the same time adequate stiffness characteristics allowing for frequency tuning with the lowest possible compression loads.

In the demonstrator, the axial stress resulting from a pre-compression load of 45 kN was -124 MPa. This compression stress is a side benefit because it tends to improve fatigue life, which represents a critical issue in MVA design. Obviously, only through a detailed assessment of the actual MVA duty cycles one can evaluate the fatigue life credit which could be achieved.

A second crucial point, as was briefly mentioned earlier, is the need to use the most efficient tension element. This means a tension link which behaves as closely as possible as a perfect string with no bending stiffness, so that during vibration it does not introduce unwanted effects, i.e. moments and curvatures which degrade the frequency-tuning effect for a given axial load.

A further point to be addressed is the adoption of a powered actuation for the axial load application. This could be relatively easily provided through a servo unit combining an electrical motor with a planetary gearbox for torque amplification; an example is illustrated in Figure 28.

Another remark stems from the observation that the system achieves frequency tuning through the modulation of a load state in the TMVA. This fact could be exploited by an alternative actuation concept where the actuator resides in the fixed frame and the load is transferred to the rotating frame through a thrust bearing. This arrangement would avoid the need to transfer electrical power to the rotor through slip rings.

Finally, as far as control is concerned, a relatively simple controller would read the rpm (and thus the N/rev frequency) and then adapt the TMVA accordingly by adjusting the actuator torque until the load cell reading matches the required value from the calibration curve. The rpm value is readily available on helicopters through an encoder.

The servo actuator could be powered through a slipring, a rechargeable battery or possibly even through an energy harvester located on the MVA mass.

MVAs, by their very nature, are continuously subjected to high accelerations in the 20-30 g range, thus they represent an ideal environment e.g. for a piezo harvester, which could extract significant vibration energy to charge a battery or supercapacitor.

The energy harvesting concept could be well suited to this application especially if we consider the peculiar nature of the duty cycles. In-fact the TMVA would need to be actuated only occasionally, through power bursts applying or releasing torque when the mission profile dictates a change of rotor rpm, thus with low actuation frequency.

Figure 28: Compact high-torque servo actuator
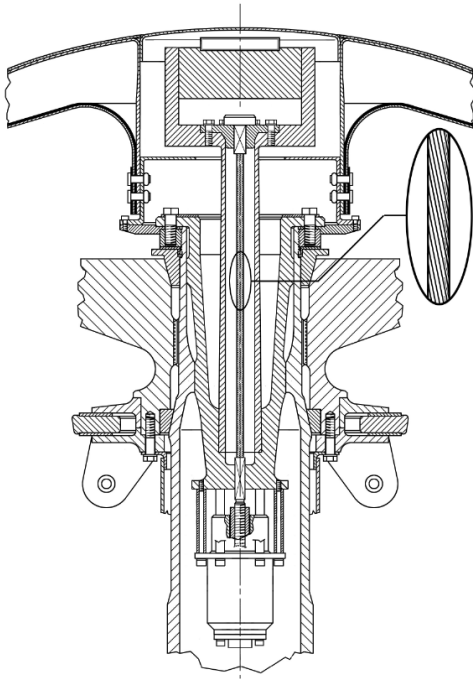
Figure 29: Scheme of tunable MVA installed on rotor mast

Figure 29 illustrates a notional installation on a rotor mast, complete with servo actuator.

In summary, the illustrated system would offer frequency tunability and rapid response in a relatively simple design.

The concept of the TMVA has been translated into a European patent filing (EP16156780.5)[12].

References

[1] Julien Austruy. *Rotor Hub Vibration and Blade Loads Reduction, and Energy Harvesting via Embedded Radial Oscillator*. Department of Aerospace Engineering, Graduate School, The Pennsylvania State University, 2011.

[2] T. Irvine. *Bending Frequencies of Beams, Rods and Pipes - Revision S*. Vibration Data, 2012.

[3] Shrikant B. Joshi. *Vibration Study of Magnetorheological Fluid Filled Sandwich Beam*. Department of Mechanical Engineering, SVERI's College of Engineering, Pandharpur, Maharashtra, India, 2012.

[4] Carmel Majid and Robert J. Wood. *Tunable Elastic Stiffness with Microconfined Magnetorheological Domains at Low Magnetic Field*. School of Engineering and Applied Sciences (SEAS), Harvard University, Cambridge, Massachusetts, 2010.

[5] Guangqiang Yang. *Large-Scale Magnetorheological Fluid Damper for Vibration Mitigation: Modeling, Testing and Control*. Department of Civil Engineering and Geological Sciences, University of Notre Dame, Indiana, 2001.

[6] Marke Kallio. *The Elastic and Damping Properties of Magnetorheological Elastomers*. VTT Technical Research Centre of Finland, 2005.

[7] R. Tao. *Super-Strong Magnetorheological Fluids*. Journal of Physics, Condensed Matter, 2001.

[8] Stephen M. Heinrich and Isabelle Dufour. *End Mass Effect On The Frequency Response Of Cantilevers: Analytical Results*. Proceedings of the 11th Nanomechanical Sensing Workshop, Madrid, Spain, 2014.

[9] Francis Shaker. *Effect of Axial Load on Mode Shapes and Frequencies of Beams*. NASA Technical Note D-8109, 1975.

[10] Stanislav Kukla and Bogdan Skalmierskir. *The Effect of Axial Loads on Transverse Vibrations of an Euler-Bernoulli Beam*. Journal of Theoretical and Applied Mechanics, 1993.

[11] Seyed Amir Mousavi Lajimi and Glenn R. Heppler. *Free Vibration and Buckling of Cantilever Beams Under Linearly Varying Axial Load Carrying an Eccentric End Rigid Body*. CSME, 1996.

[12] Luigi M. Bottasso. *Patent Filing EP16156780.5: Dispositivo di Smorzamento e Metodo di Smorzamento delle Vibrazioni per un Rotore di un Aeromobile in Grado di Volare a Punto Fisso*. Leonardo Finmeccanica, 2016.